Diffuse optical tomography of breast cancer during neoadjuvant chemotherapy: A case study with comparison to MRI

Regine Choe,[a)] Alper Corlu, Kijoon Lee, Turgut Durduran,
Soren D. Konecky, and Monika Grosicka-Koptyra
*Department of Physics and Astronomy, University of Pennsylvania, 209 South 33rd Street, Philadelphia,
Pennsylvania 19104-6396*

Simon R. Arridge
Department of Computer Science, University College London, London, WC1E 6BT, United Kingdom

Brian J. Czerniecki and Douglas L. Fraker
*Department of Surgery, Hospital of the University of Pennsylvania, 3400 Spruce Street, Philadelphia,
Pennsylvania 19104*

Angela DeMichele
*Department of Medicine (Heme/Onc), Hospital of the University of Pennsylvania, 3400 Spruce Street,
Philadelphia, Pennsylvania 19104*

Britton Chance
*Department of Biochemistry and Biophysics, University of Pennsylvania, 3620 Hamilton Walk, Philadelphia,
Pennsylvania 19104*

Mark A. Rosen
*Department of Radiology, Hospital of the University of Pennsylvania, 3400 Spruce Street, Philadelphia,
Pennsylvania 19104*

Arjun G. Yodh
*Department of Physics and Astronomy, University of Pennsylvania, 209 South 33rd Street, Philadelphia,
Pennsylvania 19104-6396*

We employ diffuse optical tomography (DOT) to track treatment progress in a female subject presenting with locally advanced invasive carcinoma of the breast during neoadjuvant chemotherapy. Three-dimensional images of total hemoglobin concentration and scattering identified the tumor. Our measurements reveal tumor shrinkage during the course of chemotherapy, in reasonable agreement with magnetic resonance images of the same subject. A decrease in total hemoglobin concentration contrast between tumor and normal tissue was also observed over time. The results demonstrate the potential of DOT for measuring physiological parameters of breast lesions during chemotherapy. © *2005 American Association of Physicists in Medicine*.
[DOI: 10.1118/1.1869612]

I. INTRODUCTION

Neoadjuvant chemotherapy (i.e., preoperative chemotherapy) is an important therapeutic approach for women with locally advanced breast cancer (LABC). LABC generally refers to lesions larger than 5 cm that may or may not have spread beyond the breast and axillary lymph nodes. If the patient responds to neoadjuvant chemotherapy, the size of the primary tumor decreases, facilitating better control through surgery while potentially eradicating micrometastatic disease.[1] Neoadjuvant chemotherapy enables a higher percentage of patients to undergo breast conservation therapy without negatively impacting local recurrence rates or long-term outcome when compared with adjuvant chemotherapy.[2] Additionally, the neoadjuvant setting provides a means to monitor the effectiveness of chemotherapy by observing its effects on the primary tumor *in vivo*.

Information about tumor response during chemotherapy may be useful for treatment optimization. Physical examination, as well as mammographic and ultrasonographic evaluations sometimes have limited utility for assessing tumor response due to chemotherapy-induced fibrosis.[3–5] While magnetic resonance imaging (MRI) has proved useful for defining the extent of residual disease when compared with pathology,[6,7] and while dynamic contrast-enhanced magnetic resonance imaging (DCE-MRI) has demonstrated ability to monitor tumor size and vascularity during neoadjuvant chemotherapy using gadolinium contrast agents,[7–9] the high cost and invasiveness of these methods render them impractical for frequent (e.g., daily) monitoring. Frequent monitoring of vascularity is important. Indeed a reduction of tumor angiogenesis from neoadjuvant chemotherapy in combination with hormone therapy has been confirmed by pathologic

analysis.[10] Therefore, new noninvasive imaging methods with capabilities for monitoring vascularity responses to neoadjuvant chemotherapy are desirable.

Diffuse optical tomography (DOT)[11] is a relatively new imaging modality with potential to follow therapy at shorter time intervals. DOT provides physiological information directly related to tumor vascularity and oxygenation, with inexpensive, nonionizing, and noninvasive instrumentation. DOT utilizes light sources in the near-infrared spectral region (600–1000 nm) wherein the major tissue chromophores are oxy-hemoglobin (HbO$_2$), deoxy-hemoglobin (Hb), water, and lipid. In this regime, photon transport is dominated by scattering, and light can penetrate centimeters (e.g., 10 cm) below the tissue surface. Using optical measurements at multiple source-detector positions on the tissue surfaces, one can readily reconstruct the internal distribution of the absorption coefficient (μ_a) and the reduced scattering coefficient (μ_s') in three dimensions. Physiological images of total hemoglobin concentration, blood oxygenation, water, and lipids are derived from this information. Thus far DOT has been applied in breast cancer imaging,[12–23] brain functional imaging,[25,27] stroke detection,[24,26] muscle functional study,[28,29] photodynamic therapy,[30,31] and radiation therapy monitoring.[68]

Not surprisingly, use of DOT for detection and characterization of breast cancer has been of great recent interest.[14,17–22,32–41] The functional information provided by DOT is complimentary to the morphological information obtained by traditional breast imaging modalities (i.e., x-ray mammogram, ultrasound, MRI). For example, clinical studies employing three-dimensional DOT have identified and quantified total hemoglobin concentration in human breast cancer,[18,32] correlating well with histologic parameters (e.g., blood vessel density).[14] Jakubowski *et al.*[41] have recently demonstrated the capability of diffuse optical *spectroscopy* (i.e., as opposed to diffuse optical *imaging*) for monitoring neoadjuvant chemotherapy in a breast cancer patient. This important paper introduced a new clinical application to the field. However, quantification of breast cancer properties from spectroscopic data alone requires assumptions about tissues (e.g., homogeneous media, etc.) which are often questionable.[42] In addition, the remission measurement geometry used in their experiments is primarily sensitive to palpable, near-surface tumors.

The potential of diffuse optical *imaging* as a chemotherapy monitoring tool has not yet been explored, and is the subject of this contribution. We present a case study which demonstrates the feasibility of this approach. We have utilized a four-wavelength near-infrared hybrid DOT instrument with continuous wave transmission and frequency-domain remission detection for breast imaging.[12] Our subject had a locally advanced invasive ductal carcinoma, and underwent four cycles of adriamycin plus cytoxan and four cycles of taxotere prior to surgery. DCE-MRI were performed at three time points throughout the therapy. After completion of adriamycin cycles, we tracked the subject with DOT at three time points. Three-dimensional DOT images of total hemoglobin concentration, oxygenation, and scattering were re-
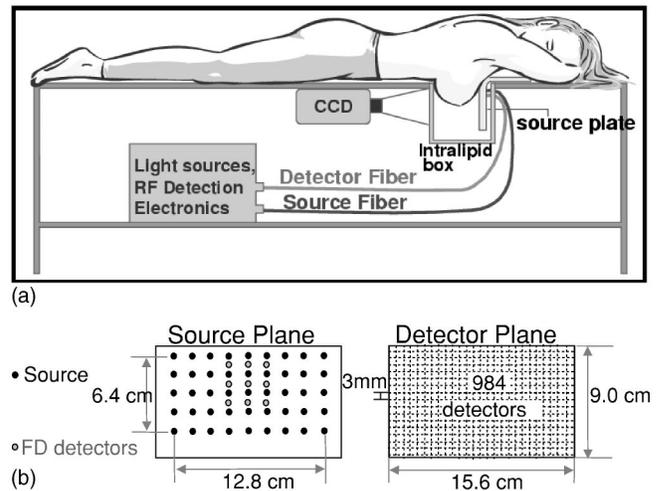

FIG. 1. Schematic of parallel plate diffuse optical tomography instrument. (a) Frequency-domain (FD) remission and continuous-wave transmission measurements were performed simultaneously on a female subject lying in prone position. (b) The source plate contains 45 source positions and 9 FD detectors. 984 detection points with 3 mm spacing were selected from CCD data for image reconstruction.

constructed. We found that tumor volume and total hemoglobin tumor-to-normal contrast decreased over the course of neoadjuvant chemotherapy. Furthermore, tumor volume changes measured by DOT showed good correlation with DCE-MRI measurements of the same subject.

II. METHODS

A. DOT instrumentation

A schematic of the DOT instrument is shown in Fig. 1. This parallel-plane DOT system has been extensively characterized for breast cancer imaging using tissue phantoms and normal breast.[12] The hybrid system combines frequency-domain (FD) remission and continuous-wave (CW) transmission detection. We briefly summarize the salient details of this instrumentation below.

The table was designed to accommodate the female subject in prone position with her breasts inside the breast box. A breast is typically centered and softly compressed between a movable compression plate and a viewing window with the compression distance ranging from 5.5 to 7.5 cm. The breast box was coated black and designed to hold a matching fluid which has optical properties similar to human tissue. The matching fluid was composed of Liposyn III (30%, Abbott Laboratories, Chicago, IL) as a scattering agent and India ink (Black India 4415, Sanford, Bellwood, IL) as an absorption agent.

Four laser diode sources, operating at 690, 750, 786, and 830 nm, respectively, were sinusoidally intensity modulated at 70 MHz. A series of optical switches (DiCon Fiber Optics, Richmond, CA) were used to direct the light sources into different source positions on the compression plate which contained 45 fibers arranged in a 9×5 grid as shown in Fig 1(b). Nine 3 mm diameter detection fiber bundles were interlaced in a 3×3 grid on the compression plate and connected
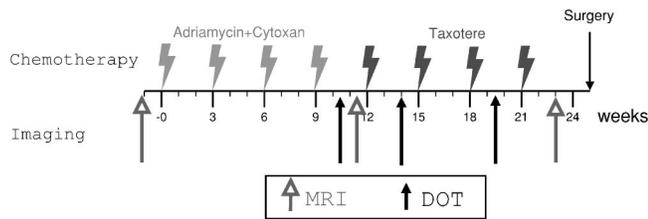
FIG. 2. Neoadjuvant chemotherapy timing diagram. Four cycles of *AC* (adriamycin+cytoxan) therapy were followed by four cycles of taxotere therapy, and then by a mastectomy. Arrows indicate timing of MRI and DOT measurements.
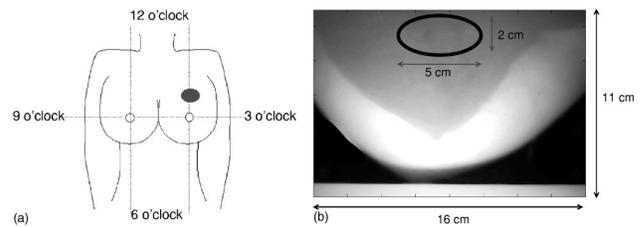

FIG. 3. Tumor location. (a) According to x-ray mammogram, ultrasound, and MRI, the primary tumor was located at the 12 o'clock position in the left breast. (b) Photo of breast outline in caudal-cranial view (foot to head view). The location of the tumor was approximated by palpation prior to DOT measurement and is indicated by a circle.

to the frequency-domain detection module. Homodyne techniques[43] were utilized to extract the amplitude and phase of the detected remission signal. The frequency-domain measurements provided accurate quantification of bulk properties of the human tissue and matching fluid, thus improving the initial guess used for the image reconstruction.

A lens-coupled 16-bit charge-coupled device (CCD) camera (Roper Scientific, Trenton, NJ, VersArray:1300F, 1340 $\times$ 1300 pixel) system with an antireflection coated glass viewing window was used for collecting CW transmission data. 2×2 on-chip binning of the CCD gave 570 $\times$ 400 pixels over a detection area of 15.6×9.0 cm.

B. Neoadjuvant chemotherapy and MRI protocol

A 35-year-old premenopausal Caucasian female underwent neoadjuvant chemotherapy for invasive ductal carcinoma in her left breast at the Hospital of the University of Pennsylvania (Philadelphia, PA). The therapy consisted of four cycles of doxorubicin (adriamycin, 60 mg/m^2) plus cyclophos-phamide (cytoxan, 600 mg/m^2, regimen denoted as *AC*) followed by docetaxel (taxotere, 100 mg/m^2, regimen denoted as *T*). Herein we will refer to the treatment as "*AC*" followed by "*T*." Each cycle was taken at three week intervals. She participated in the MRI research study CALGB150007/150012: "Contrast Enhanced Breast MRI and Correlative Science Studies to Characterize Tumor Response in Patients Undergoing Neoadjuvant Chemotherapy for Locally Advanced Breast Cancer (I-SPY)" (PI:L. Esserman, MD, MBA). The timing diagram for chemotherapy and imaging measurements (MRI and DOT) is provided in Fig. 2.

DCE-MRI measurements were performed at the following time points: one week before chemotherapy (prechemotherapy), week 12 following completion of *AC*, but prior to initiation of taxotere (*T*) therapy, and week 23 following the completion of taxotere therapy, but prior to surgical tumor removal (mastectomy). MRI of the breast was performed at 1.5 T (General Electric, Signa, Milwaukee, WI) using in-house sagittal compression receiver coils.[44] At each time point, the DCE-MRI measurement consisted of sagittal high-resolution thin section three-dimensional T1-weighted spoiled gradient echo imaging of the affected breast performed before, and twice following, bolus intravenous administration of 0.1 mmol/kg gadolinium diamide (Omniscan©, Nycomed, Princeton, NJ).

The patient underwent simple mastectomy following the eighth chemotherapy cycle. The surgical sample was inspected grossly and margins were inked in a standard fashion. The sample was then oriented anatomically, and sagittally sectioned to correspond to the MRI imaging plane. Gross inspection revealed an indurated area of abnormal, firm tissue in the superior breast measuring 1.5 cm in anterior-posterior dimension. This area was evaluated histologically with Hematoxylin and Eosin staining.

C. DOT protocol

Before each DOT measurement, informed consent was obtained from the patient in accordance with University of Pennsylvania Institutional Review Board. Based on the tumor location identified by palpation [Fig. 3(a)], the breast position with respect to the viewing window was optimized [Fig. 3(b)]. Then a soft compression was applied to hold the breast in a stable position. The compression distance was fixed at 7.5 cm. A snapshot of the breast outline was taken by the CCD camera before filling the box with the matching fluid [Fig. 3(b)]. After filling, the diffuse optical image scan was conducted for 12 min. After human subject measurements, reference optical measurements were performed on the box filled completely with matching fluid. For the reference measurements, a silicone (RTV12 with carbon black and TiO$_2$) block was placed on top of the box to extend the diffuse medium in a manner analogous to the subject's chest-wall, and thus avoid signal saturation due to the air boundary. DOT measurements were performed at 10, 14, and 19 weeks after the first *AC* cycle (see Fig. 2). These time points correspond to after the fourth *AC* (fourth chemotherapy), the first taxotere (fifth chemotherapy), and the third taxotere chemotherapy cycles (seventh chemotherapy), respectively.

D. MRI data analysis

Tumor measurements by MRI were performed through analysis of enhancing tumor pixels. Subtraction imaging (post-gadolinium minus pregadolinium) was employed as required. Maximum intensity projections in the sagittal and axial planes were obtained to facilitate accurate tumor measurement in three orthogonal dimensions. A radiologist with

Transillumination at 830 nm

After 4th
Chemotherapy

After 5th
Chemotherapy
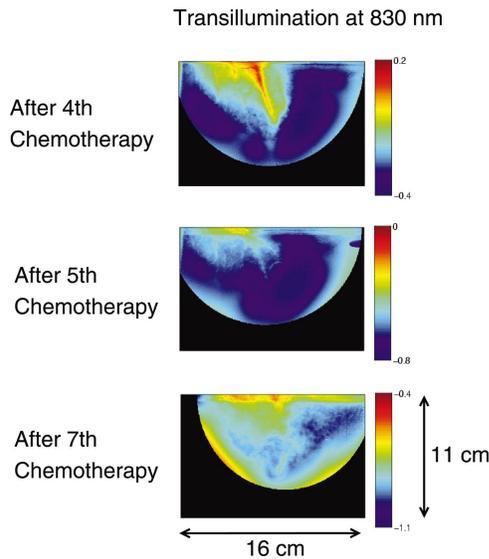
After 7th
Chemotherapy

11 cm

16 cm

FIG. 4. Transillumination of breast at 830 nm normalized with respect to reference measurement, offering a composite view of attenuation level.

breast MRI experience measured the tumor in three orthogonal planes. Tumor volume was then computed assuming an ellipsoid shape.

E. DOT transillumination

The sequential nature of data acquisition produces a set of two-dimensional (2D) continuous wave CCD intensity maps. We define the detected intensity at detection position $\mathbf{r}_d$ due to source number s to be $I(s, \mathbf{r}_d)$. A two-dimensional *transillumination* picture is constructed by summing the contribution of all sources, and normalizing with reference data $I^0(s, \mathbf{r}_d)$, i.e.,

$$T(\mathbf{r}_d) = -\log\left(\frac{\sum_s^{N_s} I(s, \mathbf{r}_d)}{\sum_s^{N_s} I^0(s, \mathbf{r}_d)} \right). \quad (1)$$

Figure 4 shows transillumination pictures after fourth, fifth, and seventh chemotherapy cycle.

The transillumination picture offers a quick composite look at the attenuation level of the raw breast data with respect to the reference data. It also enabled us to identify surface features which may correlate with image artifacts.

F. DOT data analysis: 3D reconstruction

Three-dimensional (3D) images are derived from the data using the diffusion model. The propagation of near-infrared light in biological tissue can be modeled by a photon diffusion equation.[45–47] For the continuous wave case, the photon transport description simplifies to the following equation:

$$\nabla \cdot [D(\mathbf{r}, \lambda) \nabla \Phi(\mathbf{r}, \lambda)] - \mu_a(\mathbf{r}, \lambda)\Phi(\mathbf{r}, \lambda) = -S(\mathbf{r}, \lambda). \quad (2)$$

Here $\mathbf{r}$ denotes position in space, $D(\mathbf{r}, \lambda) \cong [1/3\mu_s'(\mathbf{r}, \lambda)]$ (Ref. 48) is the light diffusion coefficient, $\mu_s'(\mathbf{r}, \lambda)$ is the reduced scattering coefficient, $\mu_a(\mathbf{r}, \lambda)$ is the absorption coefficient, $\Phi(\mathbf{r}, \lambda)$ is the photon fluence rate ($[\text{W/m}^2]$), and

$S(\mathbf{r}, \lambda)$ is the isotropic light source term ($[\text{W/m}^3]$) with wavelength λ. The absorption coefficient $\mu_a(\mathbf{r}, \lambda)$ and reduced scattering coefficient $\mu_s'(\mathbf{r}, \lambda)$ are the two most important parameters connecting the diffusion model to tissue physiology via the relations: $\mu_a(\mathbf{r}, \lambda) = \Sigma_{l=1}^L \epsilon_l(\lambda) C_l(\mathbf{r}) + \mu_a^{\text{background}}(\mathbf{r}, \lambda)$ and $\mu_s'(\mathbf{r}, \lambda) = A(\mathbf{r})\lambda^{-b(\mathbf{r})}$. Here we assume L chromophores contribute to absorption, each with extinction coefficient $\epsilon_l(\lambda)$ and concentration $C_l(\mathbf{r})$. The scattering prefactor $A(\mathbf{r})$ and scattering power $b(\mathbf{r})$ give information about the size and density distribution of scatterers in tissue.[49,50]

For image reconstruction we start with some initial distribution of $C_l(\mathbf{r})$, $A(\mathbf{r})$, and $b(\mathbf{r})$, and then solve Eq. (2) for $\Phi(\mathbf{r}, \lambda)$ using a finite element (FEM) based numerical solver.[51] We next update these parameters using a multispectral inverse approach[52,53] until good agreement between the calculated $\Phi_c(\mathbf{r}, \lambda)$ and measured $\Phi_m(\mathbf{r}, \lambda)$ fluence rates on the boundaries is obtained. Specifically, the update process is treated as an optimization problem where an objective function

$$\chi^2 = \frac{1}{2} \sum_{n=1}^N \sum_{j=1}^S \sum_{i=1}^{M_j} \left[\log\left(\frac{\Phi_m(\mathbf{r}_i, \mathbf{r}_j, \lambda_n)}{\Phi_m^0(\mathbf{r}_i, \mathbf{r}_j, \lambda_n)} \frac{\Phi_c^0(\mathbf{r}_i, \mathbf{r}_j, \lambda_n)}{\Phi_c(\mathbf{r}_i, \mathbf{r}_j, \lambda_n)} \right) \right]^2, \quad (3)$$

is minimized iteratively using a gradient-based scheme[54] suited to the multispectral method.[52,53] Here N is the total number of measurement wavelengths, S is the total number of sources, and M_j is the number of detectors corresponding to source j above the noise floor. $\mathbf{r}_i$ is the ith detector position and $\mathbf{r}_j$ is the jth source position. Φ_m^0 and Φ_c^0 are the measured and calculated fluence for reference measurements, respectively, with the breast box entirely filled with matching fluid. The objective function is then modified to incorporate spatially variant regularization[12,55] with an envelope-guided approach[56] where regularization parameters are optimized within the overall iterative process.[57]

The reconstruction volume was a $16 \text{ cm} \times 7.5 \text{ cm} \times 16 \text{ cm}$ region, extending into the chestwall area. In this volume, a finite element mesh with 58087 nodes was used by the finite element method based forward solver to calculate Φ_c. Φ_m was constructed by sampling and smoothing the CCD data on a 41×24 grid [total 984 detection points, Fig. 1(b)] with 3 mm spacing for each source. Hemoglobin concentrations $C_{\text{Hb}}(\mathbf{r})$, $C_{\text{HbO}_2}(\mathbf{r})$, and the scattering prefactor $A(\mathbf{r})$ were chosen as unknowns to be reconstructed while other variables such as water concentration $C_{\text{H}_2\text{O}}(\mathbf{r})$ and lipid concentration $C_{\text{lipid}}(\mathbf{r})$ and scattering power, $b(\mathbf{r})$ were fixed as described below.

Since our particular imaging geometry involves space occupied by both breast and matching fluid, image segmentation of the breast and matching fluid was used throughout our calculations. The breast region was approximated as a three-dimensional (3D) half-ellipsoid based on its outline in the photograph taken prior to the measurement scan [Fig. 3(b)]. To assign background and initial values to the two regions, bulk optical properties of the matching fluid were derived from frequency-domain reference measurements made on the box when it was completely filled with match-
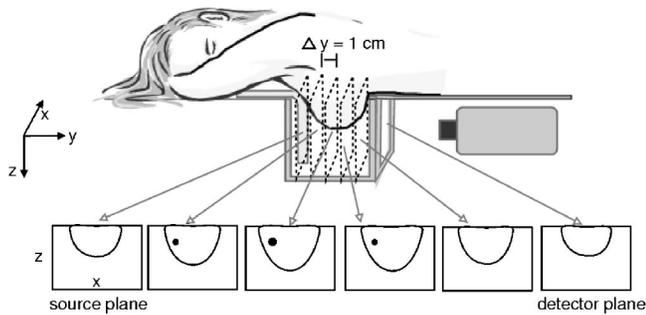
FIG. 5. Orientation of three-dimensional reconstructed DOT images. Caudal-cranial slices (foot to head) were arranged left to right, from source to detector plane. The left side of each image is lateral and right side is medial.
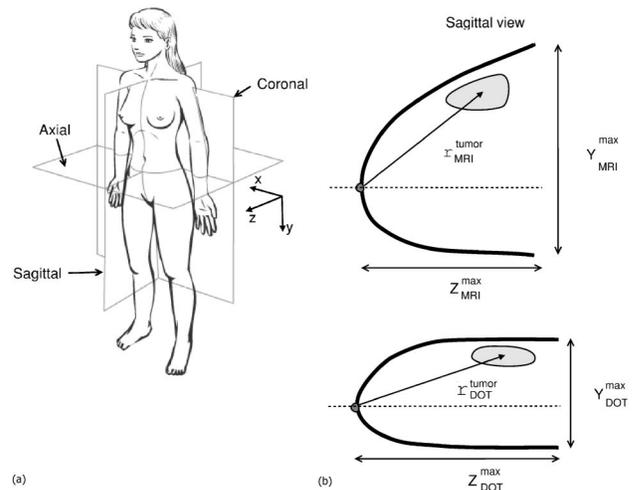

FIG. 6. (a) Orientation of MRI view. (b) A sagittal view of MRI (top) and DOT (bottom) showing differences in compression. A linear scaling transformation scheme was utilized to find the tumor center with respect to the nipple in DOT image ($\mathbf{r}_{DOT}^{tumor}$) from MRI $\mathbf{r}_{MRI}^{tumor}$.

ing fluid. The breast optical properties were derived from frequency-domain measurements in contact with breast surface. A homogeneous semi-infinite analytic solution of the frequency-domain diffusion equation with a multispectral approach[58] was utilized to fit directly for the bulk C_{Hb}, C_{HbO_2}, C_{H_2O}, A, and b in each region. The scattering power b was allowed to take on different values in the breast and matching fluid, respectively. $\mu_a^{background}$ inside the breast was then fixed as a combination of 15% water (estimated from frequency-domain measurement of bulk C_{H_2O}) and 57% lipid absorption (from literature[59–61]). $\mu_a^{background}$ for the matching fluid region was fixed at the fitted bulk μ_a of the matching fluid. For the initial guess, C_{Hb}, C_{HbO_2}, and A were assigned to the breast and the matching fluid based on the bulk measurements, e.g., zero hemoglobin concentration in the matching fluid region. After the reconstruction of $C_{Hb}(\mathbf{r})$, $C_{HbO_2}(\mathbf{r})$, and $A(\mathbf{r})$, 3D images of total hemoglobin concentration $[THC(\mathbf{r}) = C_{Hb}(\mathbf{r}) + C_{HbO_2}(\mathbf{r})]$, blood oxygenation saturation $[StO_2(\mathbf{r}) = C_{HbO_2}(\mathbf{r})/THC(\mathbf{r})]$, and scattering $[\mu_s'(\mathbf{r},\lambda) = A(\mathbf{r})\lambda^{-b(\mathbf{r})}]$ were constructed.

G. DOT image orientation

Figure 5 shows the orientation of three-dimensional reconstructed DOT images. A series of slices along the y axis are arranged from left to right, from the source plane to the detector plane, respectively. Each slice represents a 16 ×11 cm image in the x-z plane, in a caudal-cranial view (i.e., from foot to head, same as the CCD camera view). The orientation of each image is such that the left side of each image slice is lateral (toward outer side of breast) and the right side is medial (toward middle of the breasts) for the left breast, and vice versa for the right breast. For simplicity of presentation, slices at selected intervals are presented. Since the reconstructed data at FEM nodes is interpolated to regular grid of 0.2 cm spacing, each slice has 0.2 cm pixel size in both x and z directions.

H. Image correlation analysis between MRI and DOT

As shown in Fig. 6(a), there are three standard orientation of views in tomography. Since the compression schemes of

MRI (sagittal) and DOT (axial) are different, a true one-to-one image comparison without distortion is not possible.

In order to compare the tumor positions obtained by MRI with those obtained by DOT, one must derive a transformation relating coordinates in the MRI axial image to coordinates in the DOT axial image. We developed a simple scaling transformation for this purpose, which by its nature cannot account for all of the deformations arising from breast compression in orthogonal directions. The schematic of the transformation is illustrated in Fig. 6(b). First, the breast dimensions of corresponding "central" image slices (i.e., slices containing the nipple) were compared. We derived linear scale factors from the ratio of breast length and breast width in these corresponding central slices. In particular we defined scale factors $\alpha = X_{DOT}^{max}/X_{MRI}^{max}$, $\beta = Y_{DOT}^{max}/Y_{MRI}^{max}$, and $\gamma = Z_{DOT}^{max}/Z_{MRI}^{max}$, where X_i^{max}, Y_i^{max}, Z_i^{max} is the longest linear dimension of the breast in the X, Y, Z directions of the ith (MRI or DOT) image.

We located the tumor center and tumor boundaries in the MRI image by finding the region with high intensity due to large gadolinium uptake. We then rescaled the tumor center coordinate $\mathbf{r}_{MRI}^{tumor}$ to $\mathbf{r}_{DOT}^{tumor}$ by multiplying by scaling factors (i.e., α, β, and γ). The tumor boundaries are defined in this rescaled fashion as well. Importantly, the tumor in the DOT image lies approximately within the volume defined by the rescaling based on prechemotherapy MRI. We note this scaling approach assumes linear deformation and does not account for elastic differences between tumor and surrounding tissue. Future models will be developed to account for elastic variations and deformation due to the different compression schemes.

I. DOT tumor volume estimation

To define a tumor volume in the DOT images, a threshold based on the standard deviations of the reconstructed parameters was introduced. First, DOT parameters were decom-
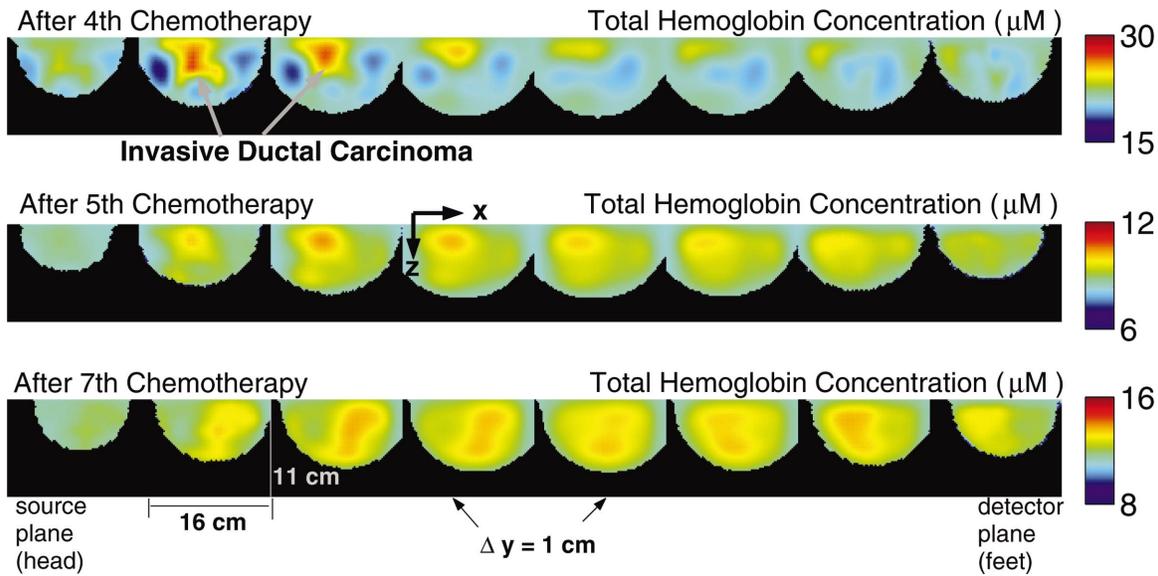
FIG. 7. Three-dimensional reconstructed total hemoglobin concentration images. Image slices from source to detection plane are presented at 1 cm intervals in caudal-cranial view, from left to right. DOT images corresponding to after 4th, 5th, and 7th chemotherapy were arranged from top to bottom.

posed into μ_a and μ_s' at 690, 750, 786, and 830 nm. Then for each image (THC, StO_2, C_{Hb}, C_{HbO_2}, and μ_a, μ_s' at the four wavelengths) an average ($\bar{p}$) and a standard deviation (σ_p) was calculated. The tumor region was defined by $p > \bar{p} + 2 \times \sigma_p$, since values greater than $2 \times \sigma_p$ have a 95% chance to be different from the average with the assumption of a Gaussian distribution. The average tumor volume (and standard deviation) was calculated by averaging all tumor regions defined by all images except StO_2 (where the variation did not exceed $2 \times \sigma_p$). Relative THC (rTHC $= THC_{tumor}/THC_{normal}$) was calculated by averaging THC in the average tumor region and outside the tumor region as

defined above. rTHC error bars were estimated based on standard deviation of THC_{tumor} and THC_{normal}.

III. RESULTS

According to the x-ray mammography, ultrasound, and MRI, the primary cancer was located at the 12 o'clock position in the left breast as shown in Fig. 3. The mammography and ultrasound reported adjacent multiple masses, the largest being $2.1 \times 2.2 \times 2.1$ cm in size at prechemotherapy time points. Prechemotherapy DCE-MRI measured the tumor size to be $5.3 \times 2.2 \times 2.7$ cm. MRI has been shown to be more
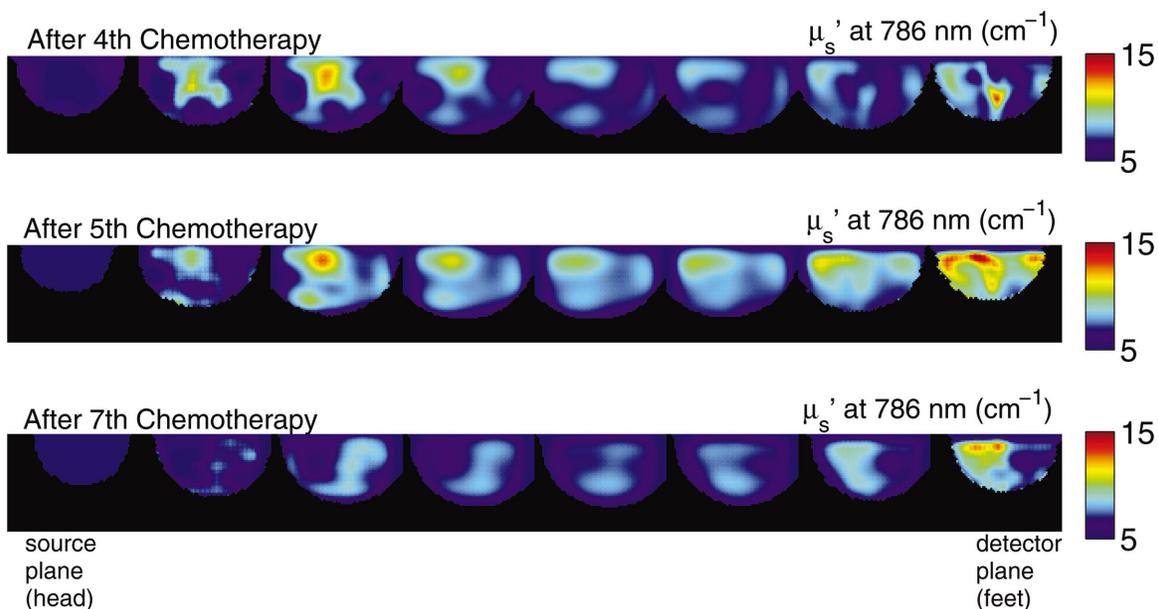

FIG. 8. Three-dimensional reconstructed images of μ_s' at 786 nm. Image slices from source to detection plane are presented at 1 cm intervals in caudal-cranial view, from left to right. DOT images corresponding to after 4th, 5th, and 7th chemotherapy were arranged from top to bottom.
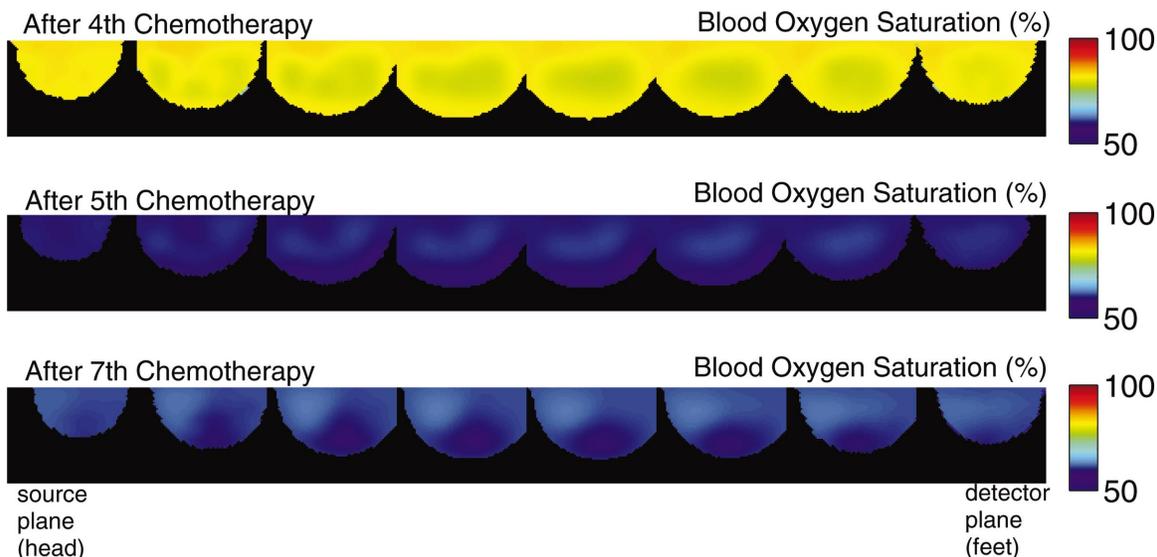
FIG. 9. Three-dimensional reconstructed blood oxygen saturation images. Image slices from source to detection plane are presented at 1 cm intervals in caudal-cranial view, from left to right. DOT images corresponding to after 4th, 5th, and 7th chemotherapy were arranged from top to bottom.

accurate in depicting the size and overall extent of tumor than mammography or ultrasound.[6,62,63] Tumor size estimation by DCE-MRI at different time points is summarized in Table I. The approximate tumor location in prone position assessed by palpation was ~8.5 cm from the nipple along the breast contour. In our camera view (caudal-cranial view), this tumor location corresponds to a distant upper central position from the nipple as shown in Fig. 3(b).

The transillumination images in Fig. 4 show high signal attenuation at the surface blood vessel and around the upper central region particularly for data taken after the fourth chemotherapy cycle. This surface blood vessel was first identified through observation while positioning and was confirmed with DCE-MRI images. The transillumination picture is quite sensitive to such surface features.

Three-dimensional DOT images of total hemoglobin concentration (THC), reduced scattering coefficient (μ'_s) at 786 nm, and blood oxygen saturation (StO$_2$) are presented in Figs. 7–9, respectively. In each figure, images from left to right correspond to 3D DOT image slices taken from source to detector planes. The DOT images corresponding to different time points within the chemotherapy cycle, are arranged from top to bottom. Color bar scales are fixed from 5 to 15 cm^{-1} for μ'_s at 786 nm, and from 50% to 100% for StO$_2$. However, colorbar scales for THC are not fixed and are

adjusted at each time point to maximize the THC color contrast between tumor and normal region. The THC scale was adjusted so its maximum value was twice its minimum value; this preserves the percentile changes in the colorbar.

In the THC images (Fig. 7) after the fourth chemotherapy cycle, a high THC region is found in slices near the source plane (1–3 cm deep from surface) and near the upper central part of the breast. The lesion position corresponds to the tumor location estimated initially by palpation at 12 o'clock and 8.5 cm away from nipple (as shown in Fig. 3). After the fifth chemotherapy cycle, the tumor region is still identified by THC contrast near the source plane and in the upper central region. However, the contrasted region appears smaller than the corresponding region after the fourth chemotherapy cycle. Also, the average THC decreased significantly (i.e., from 21.4±1.4 μM to 9.1±0.5 μM). The THC distribution after the seventh chemotherapy cycle is more homogeneous throughout the slices compared to previous chemotherapy cycles. Within the original tumor margins, the high THC region shifts toward outside of the tumor, leaving a relatively low THC region occupying most of the tumor extent. The average THC increased slightly between Figs. 7(b) and 7(c) from 9.1±0.5 μM to 12.5±0.6 μM.

Figure 8 exhibits a similar trend. It shows higher μ'_s values in the tumor region, and this region with high μ'_s shrinks over the course of treatment. The μ'_s range does not vary as dramatically as the THC, and gives a higher contrast ratio between tumor and normal tissue. Slices near the detection plane are affected by artifacts related to large vessels. These artifacts bear close resemblance to the transillumination picture in Fig. 4, which is sensitive to large blood vessels on the surface near the detection plane. This effect is also apparent in the THC images, but to a much lesser degree. Therefore, slices near the detection plane (i.e., within 1 cm) were excluded in calculations of average values of THC, StO$_2$, and μ'_s.

TABLE I. Tumor size measured with DCE-MRI at different time points during neoadjuvant chemotherapy (*AC*: adriamycin+cytoxan, *T*: taxotere). Tumor volume was estimated by assuming ellipsoidal tumor shape.

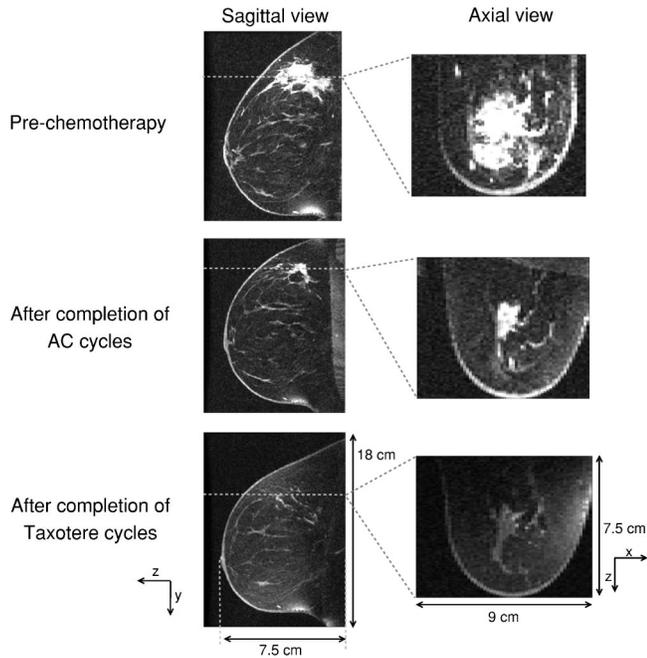| Time	Tumor size (cm)	Tumor volume (cm^3)
Prechemotherapy	5.3×2.2×2.7	16.5
After completion of *AC* cycles	3.8×1.4×1.8	5.0
After completion of *T* cycles	3.0×1.6×1.3	3.3

FIG. 10. Dynamic-contrast enhanced MRI images of left breast. From top to bottom, representative sagittal and axial slices along highest tumor contrast are shown for each time point: prechemotherapy, after completion of *AC* cycles, and after completion of taxotere cycles.
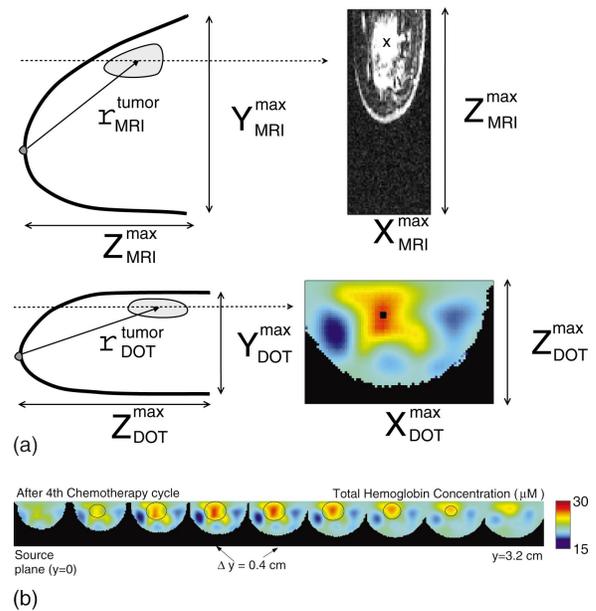

FIG. 11. Correlation of tumor position in three-dimensions. (a) Tumor center position from MRI image (a X in the axial slice) is transformed by a linear scaling scheme to the DOT coordinates (a square in the corresponding DOT axial slice). The scaled tumor center (a square) lies within a high total hemoglobin concentration region. (b) The scaled tumor boundaries around the tumor center is superimposed in three-dimensional DOT images. Axial images shown with smaller *y* intervals (0.4 cm) show the extent of the tumor in detail.

StO_2 images in Fig. 9 were relatively homogeneous and do not show contrast in the tumor region (i.e., not exceeding $2 \times \sigma_p$). Note, however, the overall StO_2 value decreased significantly after the fifth chemotherapy cycle and remained constant thereafter (i.e., from $81.2\% \pm 1.4\%$ to $59.9\% \pm 0.6\%$ to $61.1\% \pm 1.0\%$).

MRI images projected in sagittal and axial views are shown in Fig. 10 for the prechemotherapy point, after *AC* therapy (week 12) and after taxotere therapy (week 23). The intensity ranges were fixed among images at different time points. The intensity of the DCE-MRI image is higher in the tumor due to increased tumor vascularity and gadolinium contrast uptake. Before chemotherapy, the tumor is clearly seen around 12 o'clock to 1 o'clock (upper quadrant in sagittal view, near center in axial view). After completion of chemotherapy cycles, the size and intensity of the enhancing region decreased significantly. Upon completion of chemotherapy, MRI demonstrated an amorphous 5–6 cm nonenhancing soft tissue region with only a scattered punctate form of enhancement. The majority of the visible mass at this time point was poorly enhancing and was deemed to represent fibrosis. The tumor position and volume measured by DCE-MRI is summarized in Table I.

Histology revealed extensive fibrosis with focal areas of inflammation, but with few vessels. However, viable tumor cells, morphologically identical to the original core biopsy specimen (obtained prior to chemotherapy) were identified. They were diffusely scattered throughout the fibrotic region as individual cells and small groups. No macroscopical viable tumor mass was identified.

In both MRI and DOT, the tumor was found in 12 o'clock, many centimeters away from the nipple. In an attempt to assess the correlation between MRI and DOT images, the simple scaling transformation scheme described earlier was performed with the assumption that nipple and tumor center are good common reference points. The DOT axial image slice corresponding to rescaled tumor center $\mathbf{r}_{DOT}^{tumor}$ (with respect to nipple position) is shown along with the corresponding MRI axial image slice in Fig. 11(a). The tumor center found in MRI (X) and DOT (square) agrees well with employment of this transformation. To show the extent of the tumor in detail, the axial DOT images with smaller *y* intervals (0.4 cm) are shown in Fig. 11(b). Higher THC contrast in DOT are distributed in three dimensions approximately within the tumor margins defined from the scaled MRI data.

The tumor volume was defined independently for MRI and DOT. MRI tumor volume was determined by a radiologist, whereas DOT tumor volume was determined by thresholding from the distribution of DOT parameters. Figure 12(a) shows the decrease of tumor volume with progression of chemotherapy. MRI results show the tumor size decreased significantly after completion of *AC* cycles. There is a general trend of decreasing tumor volume in MRI and DOT, respectively. The degree of change is different between MRI and DOT, but direct comparison is not possible because the measurement time-point mismatch. The coinciding time point is just after the fourth chemotherapy cycle (completion of *AC*), where tumor volume measured by DOT is greater
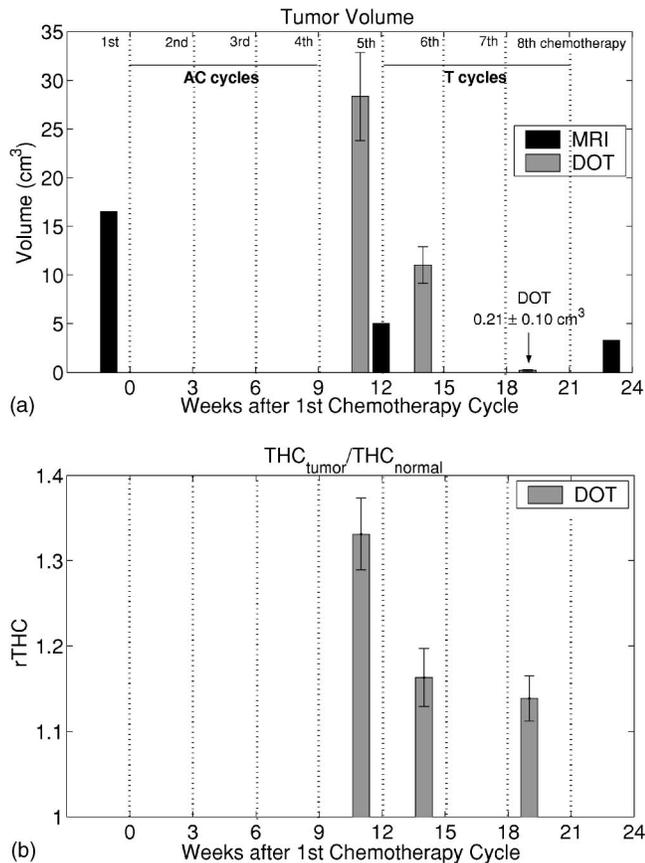
FIG. 12. (a) Decrease of tumor volume quantified by DOT and MRI, (b) Change of *r*THC in the tumor volume. Significant decrease in *r*THC is noted before and after the 5th chemotherapy.

than tumor volume measured by MRI. We note that DOT tumor volume can be overestimated due to the ill-posed nature of DOT, which introduces blurring.[12] In DOT, there was a significant tumor volume decrease in each chemotherapy cycle accompanied by *r*THC decrease in Fig. 12(b). Significant decreases of *r*THC were observed after the fifth chemotherapy cycle, which is the first taxotere chemotherapy. The *r*THC after fifth and seventh chemotherapy cycles are equivalent, but accompanied with significant tumor volume decrease, implying tumor neovasculature regression with chemotherapy.

IV. DISCUSSION

We have demonstrated three-dimensional DOT images of total hemoglobin concentration (THC), tissue blood oxygenation (StO$_2$), and scattering coefficient are useful for localizing, quantifying, and tracking breast cancer based on vascularity during neoadjuvant chemotherapy. THC and scattering showed localized contrast between the cancer and the normal region. The THC increase in tumor is expected due to angiogenesis accompanying tumor growth.[64] The enhancement of scattering might be expected based on changes in nuclear size and on the increase in concentration of organelles such as mitochondria due to the high metabolism in cancer cells.[64] Generally, StO$_2$ might have been expected to be lower in the

tumor region due to high oxygen demand, however this effect was not apparent.

The localized changes of these physiological parameters over time clearly demonstrate the dynamic imaging capability of the DOT method. The DOT measurements were carried out at time points just after completion of *AC* (adriamycin+cytoxan) cycles and then just after the first and third taxotere cycles. The antivascular and apoptotic effects of taxane[65] are consistent with the significant decrease in tumor vasculature as measured in the tumor THC contrast, the tumor volume decrease, and the intensity decrease from DCE-MRI. Interestingly, the variations in average THC appear to be qualitatively correlated with measurements of patient hematocrit over the same time period, which varied from 38% to 33% to 36%. The trends observed by DOT and MRI are consistent with pathologic findings about the effectiveness of chemotherapy. The carcinoma cells in the post-chemotherapy stage were finely and diffusely dispersed in fibrous connective tissue which represented the bulk of the residual mass. This remaining viable tumor was detected by MRI as focal enhancements and by DOT as small but positive THC contrast. Even though there was no significant spatial contrast in StO$_2$ for this subject, a significant decrease of average StO$_2$ was observed over time; this type of information might also be useful for chemotherapy monitoring, since tumor response can depend on the oxygenation of the tumor and surrounding tissues.[66,67]

Jakubowski *et al.*[41] reported THC and H$_2$O as major contrast factors, but did not report the behavior of scattering. In our case, water concentration was estimated by the frequency-domain measurements and was then fixed for continuous-wave image reconstruction. In addition to fixing the water and lipid concentration, we have tried fitting for the water concentration, but the reconstructed water concentration did not change much from its initial value. This may be because our measurements used only four wavelengths (<900 nm), all of which were outside of the water-sensitive range. As for the scattering contrast, it is possible that some portion of this signal may arise from absorption-scatter image cross-talk, since the wavelengths used to discern chromophores and scattering were not optimized.[52] The scattering artifact near the detection plane resembled the blood vessel in transillumination, and thus raises concerns about scattering-absorption cross-talk. However, our 3D simulations with noise in the same geometry find less than 20% cross-talk between THC and scattering, whereas the observed scattering contrast (averaged over tumor volume) amounts for more than a 60% increase over the normal tissues. We therefore suspect that the observed scattering contrast may indeed originate, at least partially, from tumor physiology.

To improve quantification of tumor optical contrast and validate the DOT method in clinical settings, several improvements are underway. Laser sources at optimal wavelengths for separation of chromophore contributions including water and scattering should further improve quantification accuracy. Currently, the imperfect tumor re-

gion correlation between MRI and DOT data arises because the linear approximations we have made for rescaling image do not account for the shift of tumor due to compression and deformation of the breast. Better modeling of the elastic deformation of breast in different compression geometries is under investigation. For better correlation between DOT and MRI, it would be ideal to synchronize measurement time and employ the same compression schemes. In this present study, it was not possible to synchronize DOT and MRI due to logistics of two separate research protocols and the constraints of patient availability. The improved coordination of DOT and MRI is now being performed for neoadjuvant chemotherapy patients. The measurement of additional pathologic parameters such as microvessel density or nuclei size will be invaluable in correlating with tumor vasculature and scattering factors and thus confirming DOT findings; these parameters are not routinely measured in the clinic. Finally, with respect to monitoring, more frequent DOT measurements should improve the therapeutic value of this technique.

V. CONCLUSION

We have demonstrated 3D diffuse optical tomography for monitoring physiological tumor responses during neoadjuvant chemotherapy in a single patient with a locally advanced breast cancer. We have also compared our results to dynamic contrast enhanced magnetic resonance imaging and pathologic analysis of the same patient. Three-dimensional reconstructed total hemoglobin concentration and scattering images successfully localized tumors and quantified the tumor volume decrease and the THC contrast decrease over the course of chemotherapy. These physiological parameters, measurable by DOT, may help to improve our understanding of chemotherapy mechanisms, and hold potential to play a role in assessment of treatment response.

ACKNOWLEDGMENTS

[a]Author to whom correspondence should be addressed; electronic mail: rgchoe@alumni.upenn.edu

[1]R. W. Carlson and A. M. Favret, "Multidisciplinary management of locally advanced breast cancer," Breast J. **5**(5), 303–307 (1999).

[2]B. Fisher, J. Bryant, N. Wolmark, E. Mamounas, A. Brown, E. R. Fisher, D. L. Wickerham, M. Begovic, A. DeCillis, A. Robidoux, R. G. Margolese, A. B. J. Cruz, H. J. L, A. W. Lees, N. V. Dimitrov, and B. H. D, "Effect of preoperative chemotherapy on the outcome of women with operable breast cancer," J. Clin. Oncol. **16**(8), 2672–2685 (1998).

[3]G. Cocconi, B. Di Blasio, G. Alberti, G. Bisagni, E. Botti, and G. Peracchia, "Problems in evaluating response of primary breast cancer to systemic therapy," Breast Cancer Res. Treat. **4**, 309–313 (1984).

[4]M. C. Segel, D. D. Paulus, and G. N. Hortobagyi, "Advanced primary breast cancer: Assessment at mammography of response to induction chemotherapy," Radiology **169**, 49–54 (1988).

[5]S. J. Vinnicombe, A. D. MacVica, R. L. Guy, J. P. Sloan, T. J. Powles, G. Knee, and J. E. Husband, "Primary breast cancer: Mammographic changes after neoadjuvant chemotherapy, with pathologic correlation," Radiology **198**, 333–340 (1996).

[6]L. Esserman, N. Hylton, L. Yassa, J. Barclay, S. Frankel, and E. Sickles, "Utility of magnetic resonance imaging in the management of breast cancer: Evidence for improved preoperative staging," J. Clin. Oncol. **17**(1), 110–119 (1999).

[7]P. J. Drew, M. J. Kerin, T. Mahapatra, C. Malone, J. R. T. Monson, L. W. Turnbull, and J. N. Fox, "Evaluation of response to neoadjuvant chemoradiotherapy for locally advanced breast cancer with dynamic contrast-enhanced MRI of the breast," Eur. J. Surg. Oncol. **27**, 617–620 (2001).

[8]M. V. Knopp, G. Brix, and S. L. Zeger, "MR mammography with pharmacokinetic mapping for monitoring of breast cancer treatment during neoadjuvant therapy," Magn. Reson Imaging Clin. N. Am. **2**(4), 633–658 (1994).

[9]N. Tsuboi, Y. Ogawa, T. Inomata, D. Yoshida, S. Yoshida, T. Moriki, and M. Kumon, "Changes in the findings of dynamic MRI by preoperative CAF chemotherapy for patients with breast cancer of stage II and III: Pathologic correlation,"Oncol. Rep. **6**(4), 727–732 (1999).

[10]A. Makris, T. J. Powles, S. Kakolyris, M. Dowsett, S. E. Ashley, and A. L. Harris, "Reduction in angiogenesis after neoadjuvant chemoendocrine therapy in patients with operable breast carcinoma," Cancer **85**(9), 1996–2000 (1998).

[11]A. G. Yodh and D. A. Boas, "Functional imaging with diffusing light," in *Biomedical Photonics Handbook* (CRC Press, Boca Raton, 2003), pp. 21–1 to 21–45.

[12]J. P. Culver, R. Choe, M. J. Holboke, L. Zubkov, T. Durduran, A. Slemp, V. Ntziachristos, B. Chance, and A. G. Yodh, "Three-dimensional diffuse optical tomography in the parallel plane transmission geometry: Evaluation of a hybrid frequency domain/continuous wave clinical system for breast imaging," Med. Phys. **30**, 235–247 (2003).

[13]H. Dehghani, B. W. Pogue, S. D. Jiang, B. Brooksby, and K. D. Paulsen, "Three-dimensional optical tomography: Resolution in small-object imaging," Appl. Opt. **42**, 3117–3128 (2003).

[14]B. W. Pogue, S. P. Poplack, T. O. McBride, W. A. Wells, K. S. Osterman, U. L. Osterberg, and K. D. Paulsen, "Quantitative hemoglobin tomography with diffuse near-infrared spectroscopy: Pilot results in the breast," Radiology **218**, 261–266 (2001).

[15]V. Ntziachristos and B. Chance, "Probing physiology and molecular function using optical imaging: Applications to breast cancer," Breast Cancer Res. Treat. **3**, 41–46 (2001).

[16]V. Ntziachristos, A. G. Yodh, M. Schnall, and B. Chance, "Concurrent MRI and diffuse optical tomography of breast after indocyanine green enhancement," Proc. Natl. Acad. Sci. U.S.A. **97**, 2767–2772 (2000).

[17]X. J. Gu, Q. Z. Zhang, M. Bartlett, L. Schutz, L. L. Fajardo, and H. B. Jiang, "Differentiation of cysts from solid tumors in the breast with diffuse optical tomography," Acad. Radiol. **11**, 53–60 (2004).

[18]H. Jiang, Y. Xu, N. Ifitimia, J. Eggert, K. Klove, L. Baron, and L. Fajardo, "Three-dimensional optical tomographic imaging of breast in a human subject," IEEE Trans. Med. Imaging **20**, 1334–1340 (2001).

[19]A. Li, E. L. Miller, M. E. Kilmer, T. J. Brukilacchio, T. Chaves, J. Stott, Q. Zhang, T. Wu, M. Chorlton, R. H. Moore, D. B. Kopans, and D. A. Boas, "Tomographic optical breast imaging guided by three-dimensional mammography," Appl. Opt. **42**, 5181–5190 (2003).

[20]Q. I. Zhu, M. M. Huang, N. G. Chen, K. Zarfos, B. Jagjivan, M. Kane, P. Hedge, and S. H. Kurtzman, "Ultrasound-guided optical tomographic imaging of malignant and benign breast lesions: Initial clinical results of 19 cases," Neoplasia **5**, 379–388 (2003).

[21]M. A. Franceschini, K. T. Moesta, S. Fantini, G. Gaida, E. Gratton, H. Jess, W. W. Mantulin, M. Seeber, P. M. Schlag, and M. Kaschke, "Frequency-domain techniques enhance optical mammography: Initial clinical results," Proc. Natl. Acad. Sci. U.S.A. **94**, 6468–6473 (1997).

[22]A. Pifferi, P. Taroni, A. Torricelli, F. Messina, R. Cubeddu, and G. Danesini, "Four-wavelength time-resolved optical mammography in the 680–980-nm range," Opt. Lett. **28**, 1138–1140 (2003).

[23]D. Grosenick, H. Wabnitz, K. T. Moesta, J. Mucke, M. Moller, C. Stroszczynski, J. Stossel, B. Wassermann, P. M. Schlag, and H. Rinneberg, "Concentration and oxygen saturation of haemoglobin of 50 breast tumours determined by time-domain optical mammography," Phys. Med. Biol. **49**(7), 1165–1181 (2004).

[24]J. P. Culver, T. Durduran, T. Furuya, C. Cheung, J. H. Greenberg, and A. G. Yodh, "Diffuse optical tomography of cerebral blood flow, oxygen-

ation, and metabolism in rat during focal ischemia," J. Cereb. Blood Flow Metab. **23**, 911–924 (2003).

[25]T. Durduran, G. Yu, M. G. Burnett, J. A. Detre, J. H. Greenberg, J. Wang, C. Zhou, and A. G. Yodh, "Diffuse optical measurement of blood flow, blood oxygenation, and metabolism in a human brain during sensorimotor cortex activation," Opt. Lett. **29**(15), 1766–1768 (2004).

[26]D. M. Hueber, M. A. Franceschini, H. Y. Ma, Q. Zhang, J. R. Ballesteros, S. Fantini, D. Wallace, V. Ntziachristos, and B. Chance, "Non-invasive and quantitative near-infrared haemoglobin spectrometry in the piglet brain during hypoxic stress, using a frequency-domain multidistance instrument," Phys. Med. Biol. **46**, 41–62 (2001).

[27]D. A. Boas, D. H. Brooks, E. L. Miller, C. A. DiMarzio, M. Kilmer, R. J. Gaudette, and Q. Zhang, "Imaging the body with diffuse optical tomography," IEEE Signal Process. Mag. **18**, 57–75 (2001).

[28]V. Quaresima, M. Ferrari, M. A. Franceschini, M. L. Hoimes, and S. Fantini, "Spatial distribution of vastus lateralis blood flow and oxyhemoglobin saturation measured at the end of isometric quadriceps contraction by multichannel near-infrared spectroscopy," J. Biomed. Opt. **9**, 413–420 (2004).

[29]U. Wolf, M. Wolf, J. H. Choi, L. A. Paunescu, L. P. Safonova, A. Michalos, and E. Gratton, "Mapping of hemodynamics on the human calf with near infrared spectroscopy and the influence of the adipose tissue thickness," Adv. Exp. Med. Biol. **510**, 225–230 (2003).

[30]B. C. Wilson, M. S. Patterson, and L. Lilge, "Implicit and explicit dosimetry in photodynamic therapy: A new paradigm," Lasers Med. Sci. **12**(3), 182–199 (1997).

[31]H. Wang, M. E. Putt, M. J. Emanuele, D. B. Shin, E. Glatstein, A. G. Yodh, and T. M. Busch, "Treatment-induced changes in tumor oxygenation predict photodynamic therapy outcome," Cancer Res. **64**, 7553–7561 (2004).

[32]H. Dehghani, B. W. Pogue, S. P. Poplack, and K. D. Paulsen, "Multiwavelength three-dimensional near-infrared tomography of the breast: Initial simulation, phantom, and clinical results," Appl. Opt. **42**, 135–145 (2003).

[33]H. B. Jiang, N. V. Iftimia, Y. Xu, J. A. Eggert, L. L. Fajardo, and K. L. Klove, "Near-infrared optical imaging of the breast with model-based reconstruction," Acad. Radiol. **9**, 186–194 (2002).

[34]R. L. Barbour, H. L. Graber, C. H. Schmitz, F. Tarantini, G. Khoury, D. J. Naar, T. F. Panetta, T. Lewis, and Y. Pei, "Time-frequency analysis of functional optical mammographic images," Proc. SPIE **4955**, 84–92 (2003).

[35]Q. Zhu, N. Chen, and S. H. Kurtzman, "Imaging tumor angiogenesis by use of combined near-infrared diffusive light and ultrasound," Opt. Lett. **28**, 337–339 (2003).

[36]D. Grosenick, H. Wabnitz, H. H. Rinneberg, K. T. Moesta, and P. M. Schlag, "Development of a time-domain optical mammograph and first in vivo applications," Appl. Opt. **38**, 2927–2943 (1999).

[37]D. Grosenick, K. T. Moesta, H. Wabnitz, J. Mucke, C. Stroszczynski, R. Macdonald, P. M. Schlag, and H. Rinneberg, "Time-domain optical mammography: Initial clinical results on detection and characterization of breast tumors," Appl. Opt. **42**, 3170–3186 (2003).

[38]A. Torricelli, L. Spinelli, A. Pifferi, P. Taroni, R. Cubeddu, and G. M. Danesini, "Use of a nonlinear perturbation approach for in vivo breast lesion characterization by multi-wavelength time-resolved optical mammography," Opt. Express **11**, 853–867 (2003).

[39]V. E. Pera, E. L. Heffer, H. Siebold, O. Schutz, S. Heywang-Kobrunner, L. Gotz, A. Heinig, and S. Fantini, "Spatial second-derivative image processing: An application to optical mammography to enhance the detection of breast tumors," J. Biomed. Opt. **8**, 517–524 (2003).

[40]B. J. Tromberg, N. Shah, R. Lanning, A. Cerussi, J. Espinoza, T. Pham, L. Svaasand, and J. Butler, "Non-invasive in vivo characterization of breast tumors using photon migration spectroscopy," Neoplasia **2**, 26–40 (2000).

[41]D. B. Jakubowski, A. E. Cerussi, F. Bevilacqua, N. Shah, D. Hsiang, J. Butler, and B. J. Tromberg, "Monitoring neoadjuvant chemotherapy in breast cancer using quantitative diffuse optical spectroscopy: A case study," J. Biomed. Opt. **9**, 230–238 (2004).

[42]D. A. Boas, T. J. Gaudette, G. Strangman, X. Cheng, J. J. A. Marota, and J. B. Mandeville, "The accuracy of near infrared spectroscopy and imaging during focal changes in cerebral hemodynamics," Neuroimage **13**, 76–90 (2001).

[43]Y. S. Yang, H. L. Liu, X. D. Li, and B. Chance, "Low-cost frequency-

[44]domain photon migration instrument for tissue spectroscopy, oximetry, and imaging," Opt. Eng. **36**(5), 1562–1569 (1997).

[44]E. K. Insko, T. J. Connick, M. D. Schnall, and S. G. Orel, "Multicoil array for high resolution imaging of the breast," Magn. Reson. Med. **37**(5), 778–784 (1997).

[45]A. Ishimaru, *Wave Propagation and Scattering in Random Media* (Academic Press, San Diego, 1978).

[46]K. Furutsu, "On the diffusion equation derived from the space-time transport equation," J. Opt. Soc. Am. **70**, 360–366 (1980).

[47]R. A. J. Groenhuis, H. A. Ferwerda, and J. J. Ten Bosch, "Scattering and absorption of turbid materials determined from reflection measurements. I. Theory," Appl. Opt. **22**, 2456–2462 (1983).

[48]T. Durduran, A. G. Yodh, B. Chance, and D. A. Boas, "Does the photon-diffusion coefficient depend on absorption?" J. Opt. Soc. Am. A **14**(12), 3358–3365 (1997).

[49]J. R. Mourant, T. Fuselier, J. Boyer, T. M. Johnson, and I. J. Bigio, "Predictions and measurements of scattering and absorption over broad wavelength ranges in tissue phantoms," Appl. Opt. **39**, 949–957 (1997).

[50]F. Bevilacqua, A. J. Berger, A. E. Cerussi, D. Jakubowski, and B. J. Tromberg, "Broadband absorption spectroscopy in turbid media by combined frequency-domain and steady-state methods," Appl. Opt. **39**, 6498–6507 (2000).

[51]S. R. Arridge and M. Schweiger, "Photon-measurement density functions. Part 2: Finite-element-method calculations," Appl. Opt. **34**(34), 8026–8036 (1995).

[52]A. Corlu, T. Durduran, R. Choe, M. Schweiger, E. M. C. Hillman, S. R. Arridge, and A. G. Yodh, "Uniqueness and wavelength optimization in continuous-wave multispectral diffuse optical tomography," Opt. Lett. **28**, 2339–2341 (2003).

[53]A. Corlu, R. Choe, T. Durduran, M. Schweiger, E. M. C. Hillman, S. R. Arridge, and A. G. Yodh, "Diffuse optical tomography with spectral constraints and wavelength optimization," Appl. Opt. (to be published).

[54]S. R. Arridge and M. Schweiger, "A gradient-based optimization scheme for optical tomography," Opt. Express **2**(6), 213–226 (1998).

[55]B. W. Pogue, T. O. McBride, J. Prewitt, U. L. Osterberg, and K. D. Paulsen, "Spatially variant regularization improves diffuse optical tomography," Appl. Opt. **38**, 2950–2961 (1999).

[56]L. Kaufman and A. Neumaier, "PET regularization by envelope guided conjugate gradients," IEEE Trans. Med. Imaging **15**, 385–389 (1996).

[57]A. Corlu, R. Choe, T. Durduran, K. Lee, S. D. Konecky, and A. G. Yodh, "Regularization of diffuse optical tomography images by envelope guided conjugate gradients," *OSA Technical Digest*, ThD4 (OSA, Washington, DC, 2004).

[58]T. Durduran, R. Choe, J. P. Culver, L. Zubkov, M. J. Holboke, J. Giammarco, B. Chance, and A. G. Yodh, "Bulk optical properties of healthy female breast tissue," Phys. Med. Biol. **47**, 2847–2861 (2002).

[59]H. Q. Woodard and D. R. White, "The composition of body tissues," Br. J. Radiol. **59**, 1209–1219 (1986).

[60]D. R. White, H. Q. Woodard, and S. M. Hammond, "Average soft-tissue and bone models for use in radiation dosimetry," Br. J. Radiol. **60**, 907–913 (1987).

[61]N. A. Lee, H. Rusinek, J. C. Weinreb, R. Chandra, R. C. Singer, and G. M. Newstead, "Fatty and fibroglandular tissue volumes in the breasts of women 20–83 years old: Comparison of x-ray mammography and computer-assisted MR imaging," Am. J. Radiol. **168**, 501–506 (1997).

[62]H. Mumtaz, M. A. Hall-Craggs, T. Davidson, K. Walmsley, W. Thurell, M. W. Kissin, and I. Taylor, "Staging of symptomatic primary breast cancer with MR imaging," Am. J. Roentgenol. **169**(2), 417–424 (1997).

[63]C. Boetes, R. D. Mus, R. Holland, J. O. Barentsz, S. P. Strijk, T. Wobbes, J. H. Hendriks, and S. H. Ruys, "Breast tumors: Comparative accuracy of MR imaging relative to mammography and use for demonstrating extent," Radiology **197**, 743–747 (1995).

[64]S. Thomsen and D. Tatman, "Physiological and pathological factors of human breast disease that can influence optical diagnosis," Ann. N.Y. Acad. Sci. **838**, 171–193 (1998).

[65]G. Gasparini, E. Biganzoli, E. Bonoldi, A. Morabito, M. Fanelli, and P. Boracchi, "Angiogenesis sustains tumor dormancy in patients with breast cancer treated with adjuvant chemotherapy," Breast Cancer Res. Treat. **65**, 71–75 (2001).

[66]P. Vaupel, A. Mayer, S. Briest, and M. Hockel, "Oxygenation gain factor: A novel parameter characterizing the association between hemoglobin level and the oxygenation status of breast cancers," Cancer Res. **63**, 7634–7637 (2003).

[67]P. Vaupel and M. Hockel, "Blood supply, oxygenation status and metabolic micromilieu of breast cancers: Characterization and therapeutic relevance," Int. J. Oncol. **17**(5), 869–879 (2000).

[68]U. Sunar, J. Zhang, J. Du, T. Durduran, C. Zhou, G. Yu, A. Kilger, H. Quon, R. Lustig, L. Loevner, S. Nioka, A. G. Yodh, and B. Chance, "Clinical responses of head & neck tumors to radiation therapy by NIR spectroscopy," *OSA Technical Digest*, FB7 (OSA, Washington, DC, 2004).